Mon. Not. R. Astron. Soc. **000**, 000–000 (0000) Printed 12 October 2015 (MN LATEX style file v2.2)

Spectropolarimetry of the Type Ib Supernova iPTF 13bvn: Revealing the complex explosion geometry of a stripped-envelope core-collapse supernova. ⋆

Emma Reilly[1]†, Justyn R. Maund[2,3], Dietrich Baade[4], J. Craig Wheeler[5], Jeffrey M. Silverman[5], Alejandro Clocchiatti[6], Ferdinando Patat[4], Peter Höflich[7], Jason Spyromilio[4], Lifan Wang[8] and Paula Zelaya[6]

[1] *Astrophysics Research Centre, School of Mathematics and Physics, Queens University Belfast, Belfast BT7 1NN, UK*
[2] *Department of Physics and Astronomy, The University of Sheffield, Hicks Building, Hounsfield Road, Sheffield, S3 7RH, UK*
[3] *Royal Society Research Fellow*
[4] *ESO - European Organisation for Astronomical Research in the Southern Hemisphere, Karl-Schwarzschild-Str. 2, 85748 Garching b. München, Germany*
[5] *Department of Astronomy, University of Texas at Austin, Austin, TX 78712-1205, USA*
[6] *Pontificia Universidad Católica de Chile, Avda. Libertador Bernardo O' Higgins 340, Santiago, Chile*
[7] *Department of Physics, Florida State University, Tallahassee, Florida 32306-4350, U.S.A.*
[8] *Department of Physics, Texas A&M University, College Station, Texas 77843-4242, U.S.A.*

arXiv:1510.02492v1 [astro-ph.SR] 8 Oct 2015

12 October 2015

ABSTRACT

We present six epochs of spectropolarimetric observations and one epoch of spectroscopy of the Type Ib SN iPTF 13bvn. The epochs of these observations correspond to -10 to $+61$ days with respect to the *r*-band light curve maximum. The continuum is intrinsically polarised to the 0.2-0.4% level throughout the observations, implying asphericities of $\sim$10% in the shape of the photosphere. We observe significant line polarisation associated with the spectral features of Ca II IR3, He I/Na I D, He I $\lambda\lambda 6678, 7065$, Fe II $\lambda 4924$ and O I $\lambda 7774$. We propose that an absorption feature at $\sim$ 6200Å, usually identified as Si II $\lambda 6355$, is most likely to be high velocity Hα at $-16,400\mathrm{km\ s^{-1}}$. Two distinctly polarised components, separated in velocity, are detected for both He I/Na I D and Ca II IR3 , indicating the presence of two discrete line forming regions in the ejecta in both radial velocity space and in the plane of the sky. We use the polarisation of He I $\lambda 5876$ as a tracer of sources of non-thermal excitation in the ejecta; finding that the bulk of the radioactive nickel was constrained to lie interior to $\sim 50-65\%$ of the ejecta radius. The observed polarisation is also discussed in the context of the possible progenitor system of iPTF 13bvn, with our observations favouring the explosion of a star with an extended, distorted envelope rather than a compact Wolf-Rayet star.

Key words: supernovae: general - supernovae: individual: iPTF 13bvn - techniques: polarimetric

1 Introduction

The most intriguing and mysterious aspect of the cataclysmic death of massive stars as supernovae (SNe) is the explosion mechanism itself. The driving force of the explosion is the subject of numerous theoretical models (see recent reviews in Burrows 2013 and Janka 2012), where the distinguishing feature between the models is the resulting geometry of the explosion. The vast majority of extragalactic SNe, however, are too distant for their geometries to be directly spatially resolved with currently available, or even planned, telescope facilities. Spectropolarimetry is a powerful probe of the 3D geometries of unresolved SNe and can therefore aid in pinning down the nature of the explosion.

Previous polarimetric studies have shown that departures from spherical symmetry are present in most if not all SNe (Wang & Wheeler 2008). Thermonuclear Type Ia SN explosions exhibit strong polarisation associated with absorption lines before peak luminosity, which subsequently decrease in strength as the SNe evolve. This implies that the inner ejecta are more spherical than the outer layers. Conversely, core collapse SNe (CCSNe) such as SNe 1993J, 2002ap, 2005bf and 2008D were observed to be highly polarised across particular lines and show asymmetries in the shape

⋆ Based on observations made with ESO Telescopes at the Paranal Observatory, under programme 091.D-0516.

† Email: ereilly528@qub.ac.uk

© 0000 RAS

of the photosphere on the order of $\sim$10% (Trammell et al. 1993; Tran et al. 1997; Kawabata et al. 2002; Wang et al. 2003; Maund et al. 2007b, 2009). In CCSNe, the degree of asymmetry appears to increase as the photosphere recedes into the deeper layers of the ejecta. The Type IIP SN 2004dj showed a dramatic increase in the continuum polarisation as the photosphere receded through the hydrogen layer into the core, unambiguously signalling that the explosion mechanism itself was inherently asymmetric and previously shielded from view by the hydrogen envelope at earlier times (Leonard et al. 2006). Polarimetry of SNe arising from progenitors that have been stripped of their outer hydrogen envelope probes the geometry of the explosion at early times.

iPTF 13bvn was discovered by the Intermediate Palomar Transient Factory (iPTF) (Law et al. 2009) on June 16.238 2013 in galaxy NGC 5806 (22.5 Mpc) and was classified as a Type Ib SN. According to Cao et al. (2013), the SN was discovered very early at only 0.57 days after their estimated explosion date of June 15.67 2013. The SN reached a peak maximum brightness of $M_r = -16.6$ on July 3 2013 (18 days later).

iPTF 13bvn is the first Type Ib SN for which a possible progenitor candidate has been detected; however the nature of the progenitor candidate is unclear. Cao et al. (2013) identified a blue object in HST/ACS pre-explosion observations, consistent with a single Wolf-Rayet star. This conclusion was supported by Groh et al. (2013) who constrained the initial mass to 31-35 $M_\odot$($\sim$11 $M_\odot$ pre-SN), and predicted a large ejecta mass ($\sim$8 $M_\odot$). Fremling et al. (2014) and Srivastav et al. (2014) both constrained the ejected mass to $\sim$2 $M_\odot$, which is inconsistent with the explosion of such a massive Wolf-Rayet star. Furthermore, hydrodynamical models of Bersten et al. (2014) suggested that the progenitor had a mass of 3.5 $M_\odot$ prior to the explosion and proposed an interacting binary as the progenitor channel. Reanalysis of the pre-explosion photometry and comparison with binary evolution models by Eldridge et al. (2015) also suggested that the progenitor was likely to be a low mass helium giant star (initial mass 10-20 $M_\odot$) in an interacting binary system.

Spectroscopically, iPTF 13bvn showed similarities to Type Ib SNe 2009jf, 2008D and 2007Y (Srivastav et al. 2014; Fremling et al. 2014). The light curve, however, showed a much faster decline than most Type Ib/c SNe and a lower peak brightness luminosity (Srivastav et al. 2014). Reproduction of the light curve with hydrodynamical models required 0.05-0.1 $M_\odot$ of nickel (consistent with an estimate by Srivastav et al. 2014) to be highly mixed out to the outermost layers of the ejecta to reproduce the rise time (Fremling et al. 2014; Bersten et al. 2014, but note that there may be issues with the treatment of opacity in standard models of the peaks of stripped-envelope SNe, Wheeler et al. 2015).

Here we present multi-epoch spectropolarimetry of iPTF 13bvn acquired with the European Southern Observatory (ESO) Very Large Telescope (VLT), covering from -10 to $+36$ days with respect to the *r*-band peak luminosity plus an additional epoch of spectroscopy at $+61$ days. The sections are organised as follows: the observations and data reduction are presented in Section 2; the results of the observations are presented and analysed in Sections 3 and 4, respectively. In Section 5 the results and analysis are discussed and in Section 6 we present our conclusions.

2 Observations and Data Reduction

Observations of iPTF 13bvn were acquired using the European Southern Observatory (ESO) Very Large Telescope (VLT) Antu (Unit 1) telescope and the Focal Reducer and Low Dispersion Spectrograph (FORS2) instrument in the spectropolarimetric PMOS and long-slit LSS modes (Appenzeller et al. 1998). Six epochs of spectropolarimetric data and one epoch of spectroscopic data were obtained. A log of the observations can be found in Table 1. For the polarimetric observations, the half-wavelength retarder plate was positioned at four angles $(0, 22.5, 45, 67.5^\circ)$ through two iterations, resulting in eight exposures at each epoch. Observations were acquired with the 300V grism, which provides a spectral resolution of 12Å as measured from arc lamp calibration frames. The GG435 order separation filter was used to prevent second order contamination at longer wavelengths, resulting in a final wavelength range of 4450-8650Å. The data were reduced in the standard manner using IRAF‡, following the prescription of Maund et al. (2007b), and the normalised Stokes parameters (q and u) were calculated following Patat & Romaniello (2006). The data were corrected for the wavelength dependent chromatic zero-angle offset of the retarder plate, and the polarisation spectra were further corrected for bias following Quinn et al. (2012). In order to increase the signal-to-noise level, the data were rebinned to 15Å, prior to the calculation of the Stokes parameters. Flux spectra of the SN at each epoch of polarimetry were calibrated using observations of a flux standard star with the polarimetry optics in place and the retarder plate at

Table 1. Table of VLT FORS2 observations of iPTF 13bvn

Object	Date (UT)	Exposure (s)	Mean Airmass	Epoch† (days)	S/N⋆
iPTF 13bvn	2013 06 23	8×870	1.16	-10	410
LTT 6248‡	2013 06 23	40	1.00		
iPTF 13bvn	2013 07 04	8×855	1.13	0	740
LTT 6248‡	2013 07 04	80	1.02		
iPTF 13bvn	2013 07 10	8×855	1.43	$+7$	640
LTT 6248‡	2013 07 10	45	1.40		
iPTF 13bvn	2013 07 12	8×855	1.37	$+9$	660
LTT 6248‡	2013 07 12	45	1.01		
iPTF 13bvn	2013 07 28	8×855	1.32	$+25$	350
LTT 6248‡	2013 07 28	90	1.1		
iPTF 13bvn	2013 08 08	8×855	1.68	$+36$	270
LTT 6248‡	2013 08 08	90	1.05		
iPTF 13bvn∗	2013 09 02	3×1180	1.79	$+61$	
LTT 7379∗‡	2013 09 02	3	1.08		

†Relative to the *r*-band maximum on the 3$^{\rm rd}$ July 2013, according to Cao et al. (2013)
‡Flux standard
∗ Spectroscopic observation
⋆ Average signal-to-noise ratio measured in the continuum regions (as identified in Figure 1).

‡ IRAF is distributed by the National Optical Astronomy Observatories, which are operated by the Association of Universities for Research in Astronomy, Inc., under cooperative agreement with the National Science Foundation -http://iraf.noao.edu/.

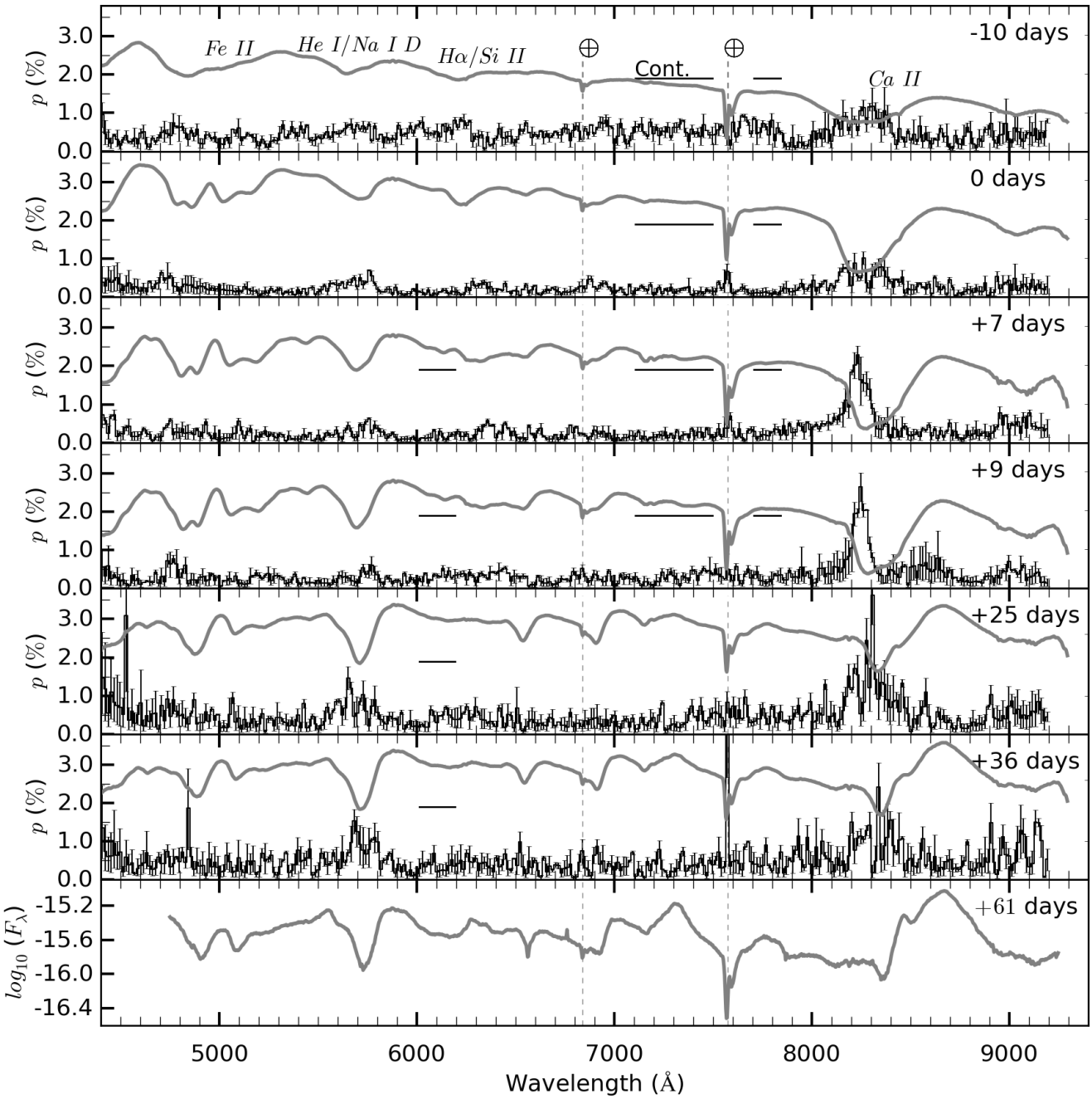

Figure 1. The polarisation spectra of iPTF 13bvn from -10 days to $+36$ days relative to the *r*-band maximum. At each epoch, the flux spectra ($log_{10}(F_\lambda)$) are shown by the thick grey lines and are corrected for the recessional velocity of the host galaxy (1359 km s^{-1}, as quoted by NED). The flux spectrum from the spectroscopic observations at $+61$ days is also shown in the bottom panel. The horizontal bars indicate the wavelength regions used to measure the continuum polarisation.

0°. The flux spectrum at $+61$ days was calibrated in the standard manner using observations of the flux standard LTT 7379.

3 Spectral Evolution

The flux spectra and degree of polarisation, p, of iPTF 13bvn for the six epochs of spectropolarimetric observations and one epoch of late time spectroscopy are presented in Figure 1. The phases indicated are with respect to the *r*-band maximum on 3 July 2013 (Cao et al. 2013).

At all epochs, the flux spectra exhibit broad P Cygni profiles of Ca II, He I and Fe II. The flux spectra are dominated by a strong absorption due to the Ca II near infrared triplet (hereafter Ca II IR3). At -10 days, the absorption exhibits a flat bottom, with a minimum at $-13{,}300$ km s^{-1}, which steadily decreases to -7450 km s^{-1} at $+36$ days. At $+7$ days the absorption becomes asymmetric, appearing to be double dipped with apparent minima at $-10{,}200$ km s^{-1} and -7000 km s^{-1}, with a blue edge extend-

ing to $-24{,}000$ km s^{-1}. By $+25$ days, the two minima occur at -4560 km s^{-1} and -8400 km s^{-1}. From $+25$ days another absorption features appears at $\sim$8125 Å , corresponding to $-16{,}200$ km s^{-1} with respect to the weighted average rest wavelength of Ca II IR3. Alternatively, this feature may be associated with a possible emission bump observed at 8169 Å. By $+61$ days, Ca II IR3 is observed to be predominantly in emission, with some evidence that the constituent lines are partially resolved. The final velocity at the absorption minimum corresponds to either -7700 km s^{-1} (assuming the weighted average rest wavelength for the triplet) or -5200 km s^{-1} (assuming the lowest rest wavelength of the individual Ca II IR3 lines 8498 Å).

Following the Ca II IR3, the next strongest feature in the spectra is the blend of He I λ5876 and Na I D at $\sim$5500-5800 Å. Over the evolution of the SN, the strength of this absorption feature increases while the velocity at the absorption minimum exhibits a slower decline compared to that observed for Ca II. The velocity decreases from $-11{,}500$ km s^{-1} at -10 days to -8800 km s^{-1} at 0 days, where it appears to plateau before settling at -7900 km s^{-1} at $+61$ days. The decay in the velocity at absorption minimum for He I/Na I D , along with Ca II IR3 and Fe II λ5169, is plotted in Figure 2. The He I/Na I D line profile appears asymmetric at early times with a blue edge extending up to $\sim -20{,}000$ km s^{-1}, and, at later epochs, there is a possible higher velocity component at $\sim -14{,}000$ km s^{-1}. He I $\lambda\lambda 6678, 7065$ are also present in the spectra, however obtaining the velocity at absorption minimum for these lines is complicated by blending with a telluric feature for He I λ7065 and with the emission component of the Si II λ6355 P Cygni profile for He I λ6678. At $+25$ and $+36$ days, the depth of the He I λ7065 absorption component is greater than that of the telluric lines, such that the velocity at minimum absorption could be measured to be -6700 and -6500 km s^{-1} at $+25$ and $+36$ days, respectively.

The absorption feature at $\sim$ 6200Å, observed at -10 days, is frequently associated with Si II λ6355. The strength of the line and the velocity of the absorption minimum decreases with time, eventually disappearing at $+25$ days. The corresponding velocity at absorption minimum of -7400 km s^{-1}, however, is lower than the photospheric velocity at the same epoch (see below and Fig. 2). Alternatively, Parrent et al. (2015) suggest that features such as this in other Type I CCSNe may be high velocity Hα. If this feature arises instead from hydrogen the corresponding velocity at absorption at -10 days was $16{,}700$ km s^{-1}.

At -10 days, Fe II is observed as an unresolved blend of doublets 38 and 42 covering the wavelength region 4800-5400 Å, before the individual lines become resolved by 0 days. Following Fremling et al. (2014), the velocity at the absorption minimum of Fe II λ5169 is used to indicate the photospheric velocity, for which we measure a velocity of -8750 km s^{-1} at 0 days. The photospheric velocity steadily decreased to -4300 km s^{-1} by $+61$ days.

O I λ7774 appears as a weak P Cygni profile from $+25$ days onwards, having been absent at earlier epochs.

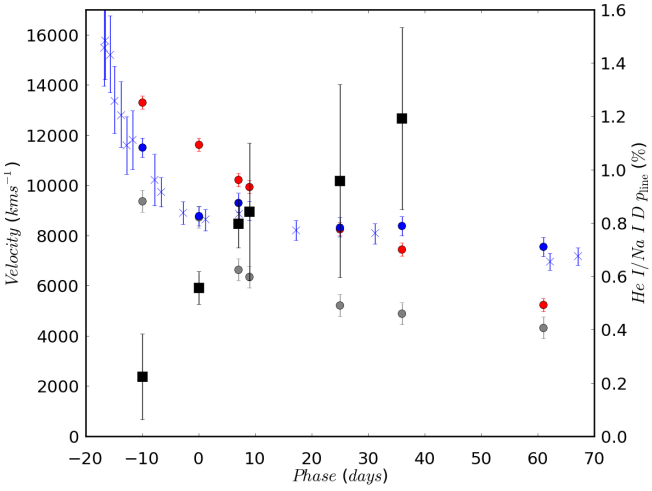

Figure 2. The evolution of the velocity at absorption minimum for Ca II IR3 (red), the He I/Na I D blend (blue) and Fe II λ5169 (a proxy for the photospheric velocity; grey). These data are marked by circles while measurements for He I/Na I D and Fe II λ5169 from Fremling et al. (2014) are also shown here by crosses. The evolution of peak line polarisation associated with the He I/Na I D blend is marked by black squares.

4 Analysis of the Polarimetry

4.1 Interstellar Polarisation

Scattering of photons due to intervening dust in the interstellar medium introduces an additional component to the observed polarisation. The removal of the interstellar polarisation (ISP) is a vital step in correctly interpreting the intrinsic polarisation of the SN. The correct determination of the ISP is non-trivial and dependent upon the assumption that certain wavelength regions of the SN spectrum are intrinsically unpolarised. One approach is to assume that resonance scattering photons are intrinsically unpolarised (Trammell et al. 1993), such as those found in strong emission lines and areas of line blanketing. Under the assumption that certain regions of the SN spectrum at certain epochs are intrinsically unpolarised and, therefore, representative of the effect of the ISP, we derive 3 estimates of the ISP:

ISP$_\mathbf{A}$: The observed polarisation for intrinsically unpolarised strong resonant scattering emission lines should tend towards the ISP (as the line strength increases). The strongest emission line in the SN spectra is the Ca II IR3 at $+36$ days. The Stokes parameters were averaged over a 60 Å range, redward of the emission peak, avoiding the polarisation associated with the blueward absorption trough. For our first estimate of the ISP, we measured values of the polarisation across this wavelength range of q_{ISP_A}=$-0.28\pm0.24\%$ and u_{ISP_A}=$0.12\pm0.25\%$.

ISP$_\mathbf{B}$: At -10 days the Fe II 38 and 42 doublets are unresolved in the spectrum leading to a region of line blanketing which is assumed to be intrinsically unpolarised. Taking the weighted average of Stokes q and u in the wavelength region 5000-5400 Å, we derive an estimate for ISP$_B$ of q_{ISP_B}=$-0.12\pm0.12\%$ and u_{ISP_B}=$0.39\pm0.14\%$.

ISP$_\mathbf{C}$: A further estimate of the ISP was determined by averaging the polarisation of the Ca II IR3 emission line and strong emission from a possible Fe II and He I blend (at $\sim$5010 Å) at $+25$ days. At this epoch the spectrum appears depolarised in these regions, from which we derive ISP$_C$ as q_{ISP_C}=$-0.19\pm0.04\%$ and u_{ISP_C}=$-0.10\pm0.08\%$.

The inverse error weighted average of the three estimates was taken as the principal estimate of the ISP, with the standard deviation as the corresponding uncertainty, resulting in q_{ISP}=$-0.19\pm0.08\%$ and u_{ISP}=$0.03\pm0.28\%$. The position of the principal and individ-

ual estimates of the ISP are shown on the Stokes $q-u$ plane on Figure 3.

The total reddening due to Galactic and host dust is $E(B-V)_{MW}$=0.0278 (Schlafly & Finkbeiner 2011) and $E(B-V)_{host}$=0.0437 (Cao et al. 2013). Assuming a Serkowski law and Galactic-type dust, this limits the degree of polarisation arising from the intervening dust to be $p_{ISP} \leqslant 9(E(B-V)_{MW}+E(B-V)_{host}) = 0.64\%$. The value we have determined for p_{ISP}= $0.25^{+0.22}_{-0.17}\%$ is therefore consistent with the maximum expected given the reddening towards tiPTF 13bvn.

4.2 Intrinsic Continuum Polarisation

The level of intrinsic continuum polarisation reveals the degree of asphericity in the SN photosphere. We identified regions of the spectrum of iPTF 13bvn at each epoch that were deemed to be flat in polarisation and far from any lines that might contaminate the polarisation (indicated by the black horizontal bars in Figure 1). As the spectrum of iPTF 13bvn evolved, with lines appearing and disappearing, the wavelength regions we considered to be representative of the continuum also changed. The continuum polarisation was measured by taking the inverse-error weighted-average of the Stokes parameters, after correction for the ISP, over the continuum wavelength ranges. The corresponding uncertainties were calculated as the standard deviation of the polarisation over the continuum wavelengths ranges, with respect to the weighted mean continuum polarisation.

We find the continuum to be intrinsically polarised at the 0.2-0.4% level throughout the series of observations. Due to the low level of polarisation, and the relatively large uncertainties ($\sim \pm 0.13\%$), there is little evidence for evolution in the degree of the continuum polarisation to the 3σ level. The continuum polarisation angle undergoes a clockwise rotation from $29\pm9^\circ$ to $177\pm3^\circ$ between the first two observations. After the second epoch, the polarisation angle remains approximately constant throughout the remaining observations of +7, +25, +36 days at $\sim$153°; however, at +9 days the continuum polarisation angle is $117\pm4^\circ$, despite no change in the degree of polarisation, at the 0.01% level, from two days before.

The inferred values for the continuum polarisation are, however, sensitive to the choice of the ISP. For example, correction for ISP_A yields similar values for the continuum polarisation as presented above, however the continuum polarisation angle at +9 days ($137 \pm 3^\circ$) is no longer discrepant from the angle measured immediately before. Upon subtraction of ISP_B, the contrinuum polarisation exhibits a steady increase from $0.19 \pm 0.10\%$ before peak brightness to $0.59 \pm 0.25\%$ at +36 days. The removal of ISP_C results in the degree of continuum polarisation reaching a maximum of $\sim$0.7% at −10 days, before decreasing to 0.13% at +7 days and then increasing again to 0.34% at +25 days. In addition, for ISP_C, the continuum polarisation angle also exhibits very dynamic behaviour changing from $32 \pm 6^\circ$ at -10 days, to $9 \pm 13^\circ$ at 0 days and then $157 \pm 20^\circ$ at +36 days.

The maximum intrinsic continuum polarisation of 0.39%, after subtraction of the averaged ISP, implies asphericities of 10% in the shape of the photosphere (Höflich 1991). For ISP_B, the maximum continuum polarisation of 0.7% implies asphericities of 10-15%. Although the different ISPs result in different continuum polarisations, the corresponding differences in the inferred shape of the photosphere are relatively small for iPTF 13bvn. The evolution in the alignment of the photosphere on the plane of the sky, however, is shown to be highly dependent on the chosen ISP.

4.3 Intrinsic Line Polarisation

The polarisation spectra, shown in Figure 1, exhibit peaks associated with the various spectral lines identified in Section 3. In the following section we analyse the temporal evolution of the line polarisation intrinsic to iPTF 13bvn. The sub-sections are organised according to species and ordered from the most strongly polarised species (Ca II) to the least (O I λ7774). The intrinsic polarisation due to line absorption features was determined with the vector subtraction of the measured continuum polarisation from the observed data. The observed continuum polarisation is the summation of the intrinsic continuum polarisation of the SN and the ISP and the subtraction of the observed continuum polarisation results, therefore, in an intrinsic line polarisation that is independent of the choice of the ISP.

4.3.1 Ca II IR3

At all epochs, the polarisation spectra are dominated by strong line polarisation associated with the Ca II IR3. The polarisation signal evolves from a broad feature (FWHM $\sim$9,500 km s^{-1}) with degree of polarisation p=0.7±0.5% at −10 days to a narrower, stronger signal of $p \sim$2.5% at +7 days. The polarisation increases again to p=3.3±0.8% at +25 days, with significant signal spread across a larger velocity range than was observed previously. The velocity at which the polarisation across the Ca II IR3 profiles appears to peak also increases from −9500 km s^{-1} at −10 days to −12,300 km s^{-1} at +7 days before decreasing again to −8400 km s^{-1} at the final epoch of spectropolarimetry. The polarisation angle (at the polarisation maximum) of Ca II is similar at −10 and 0 days, with $\theta_{\rm line} \sim 70^\circ$. It then rotates to $\sim 120^\circ$ at +7 days, where it remains throughout the rest of the observations.

There is significant structure associated with this line on the Stokes q-u plane, shown in Figure 3. At 0 days, there is a loop that crosses all quadrants of the q-u plane, with 3 separate components at $\sim$ −8000, −12,000 and −15,000 km s^{-1}, suggesting a complex line forming structure in the plane of the sky. The shape of the loop changes at +7 days, resulting in an extended loop for velocities between $\sim$ −7000 km s^{-1} and $\sim$ −15,000 km s^{-1}, while at lower velocities the signal appears to cluster near the origin of the q-u plane and at higher velocities ($\lesssim$ −15,000 km s^{-1}) the data are clustered at $\sim 135^\circ$. At +9 and +25 days the feature on the q-u plane is similar to that observed +7 days, although with a higher degree of polarisation $p \sim$3.3% seen at +25 days. There is evidence of significant polarisation at +36 days, however the signal-to-noise ratio is insufficient to properly discern any structure in the q-u plane at this epoch.

At +7 days, there is evidence of polarised flux in a blue wing to the absorption profile, that extends to velocities of $\sim$ −20,000 km s^{-1}. To determine if the blue wing is polarised in the same manner as the strong polarisation seen at $-12,300$ km s^{-1}, or due to a separate polarising component, the observed degree of polarisation ($p_{\rm obs}$) was modelled as:

$$p_{\rm obs} = \frac{p_{\rm line}F_{\rm line} + p_{\rm cont}F_{\rm cont}}{F_{\rm obs}} \quad (1)$$

where $F_{\rm line}$ and $F_{\rm cont}$ are the line and continuum fluxes, respectively, and $p_{\rm cont}$ is the continuum polarisation. These values were

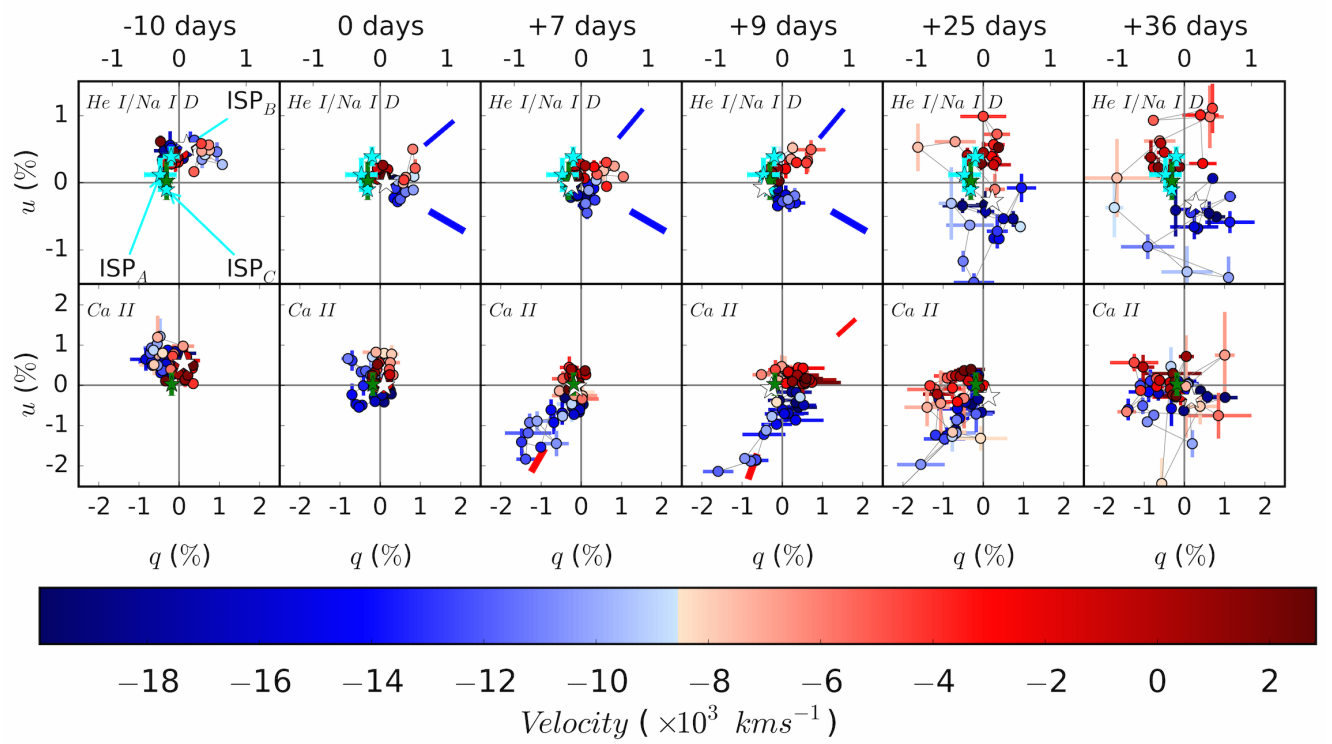

Figure 3. The observed polarisation of the He I/Na I D blend (top panel) and Ca II IR3 (bottom panel) on the Stokes q-u plane. The points are coloured coded according their velocity with respect to the rest wavelength. Radial lines indicate the principal polarisation angles for the LV (narrow lines) and HV (thick lines) components, for epochs at which they appear as separate features. The position of the measured continuum polarisation is indicated by the white star. The three individual estimates of the ISP (see Section 4.1) are marked by cyan stars and the position of the average ISP estimate is marked by the green star. Note the difference in scale between the top and bottom panels.

measured directly from the observed data. The intrinsic line polarisation, $p_{\rm line}$, was varied according to Equation 1 in order to reproduce $p_{\rm obs}$. Below $\sim -8000\,{\rm km\ s^{-1}}$, the observed polarisation is best replicated with low intrinsic polarisation, $p_{\rm line}$=0.0±0.2%, however this is not representative for the data at higher velocities. Between -8000 km s^{-1} and $-14{,}000$ km s^{-1}, $p_{\rm line}$=0.6±0.4%. For velocities higher than $\sim -14,000\,{\rm km\ s^{-1}}$, a higher degree of polarisation is required with $p_{\rm line}$=1.6±0.2%. As can be seen in Figure 4, the data could not be reproduced with a single $p_{\rm line}$ covering the entire wavelength range of the profile, indicating that a single geometrical configuration is not responsible for the polarisation profile. This suggests that the Ca II IR3 line profile actually arises from 3 different structures in the plane of the sky: a weakly polarised, strongly absorbing low velocity (LV) component; a more asymmetric, strongly absorbing, high velocity (HV) component; and a very strongly polarising, but weakly absorbing, very high velocity (V-HV) component.

The behaviour of the polarisation angle across the line profile displays an intriguing evolution. At -10 days, the polarisation remains constant as a function of velocity at $\sim$70°. By maximum light, however, we observe a steady rotation in the polarisation angle from $\sim$50° to 150° with increasing velocity. At +7 days the polarisation angle across the line profile begins to split into two separate components, with the separation between the two becoming clearly apparent by +9 days . At +9 days there is a defined break in the polarisation angle at -8100 km s^{-1} between the two components (see Figure 5). The LV component, at $\theta_{\rm line}$=21°, is separated by $\sim$75° (or -55°) from the HV component (from -8100 km s^{-1} to $\sim -15{,}000$ km s^{-1}) at $\theta_{\rm line}$=125°. At +25 days, the polarisation angle changes steadily from approximately 50° at low velocities to 120° at $-10{,}000$ km s^{-1}. The data are noisier at +36 days, however the trend in the polarisation angle appears to be similar to that observed at the previous epoch.

While separate HV and LV components are observed for Ca II in the polarised flux spectrum (at +9 days), an analysis of the Ca II IR3 line profile in the flux spectrum, following the prescription of Silverman et al. (2015), was not able to recover the two separate components. The asymmetric line profile observed in the flux spectrum, from +7 days onwards, was found to result from a superposition of the individual components of the triplet (at ~ -8800 km s^{-1}) becoming partially resolved. We note, however, that this analysis assumes that the underlying line profiles are well described by Gaussian profiles.

The fits also indicated that an additional narrow absorption feature at +25 days, at $\sim$8150 Å or $-14{,}000$ km s^{-1}relative to the Ca II IR3 rest wavelength, is probably unrelated to Ca and is probably due to another element. Although not observed at earlier epochs, the velocity of this feature places it in the "blue wing" or V-HV component of the Ca II IR3 absorption. This could suggest that the extreme line polarisation measured for the V-HV component at +9 days may not actually be due to Ca. Conversely, we note that if this separate species were responsible for the polarisation of V-HV component, the degree of polarisation would appear to be anti-correlated with the increasing strength of the line in the flux spectrum at later epochs. The presence of two components in the He I/Na I D profiles (discussed in Section 4.3.2) leads us to conclude that the separate LV and HV components Ca II are real.

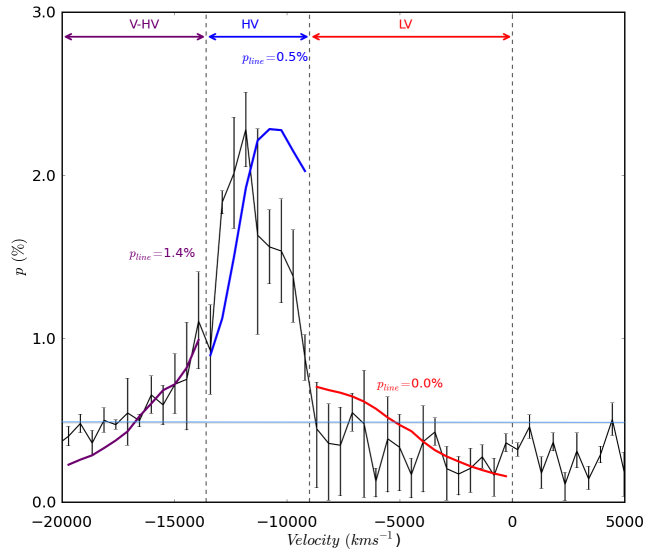

Figure 4. Fits to the observed degree of polarisation for the Ca II IR3 at +9 days with $p_{\rm line}$ as a variable. No one value of $p_{\rm line}$ can provide a complete fit to the observed polarisation across the entire line profile. The best fits to LV, HV and V-HV components of the line are marked in red, blue and purple, respectively.

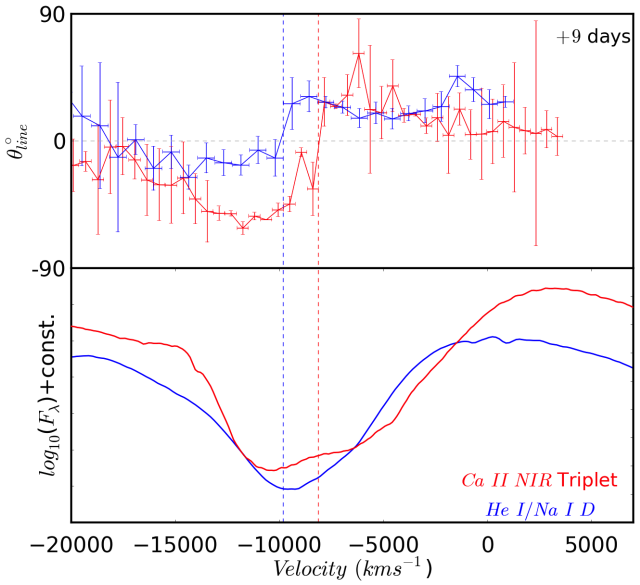

Figure 5. The polarisation angle as a function of velocity for the Ca II IR3 (red) and He I/Na I D (blue) profiles at +9 days. The bottom panel shows the total flux spectra across each of these profiles. The dashed lines represent the velocity of the transition between the LV and HV components for Ca II IR3 (red, -8100 km s^{-1}) and He I/Na I D (blue, -9800 km s^{-1}).

4.3.2 *He* I λλ5876, 6678, 7065 *and Na* I *D*

Polarisation is also associated with the He I absorption lines, most prominently seen in the He I/Na I D blend. The intrinsic degree of polarisation of the He I/Na I D blend grows from $p_{\rm line}$=0.29±0.06% at -10 days to 1.2±0.3% at the final epoch of polarimetry. At -10 days, the data points of the He I/Na I D blend cluster around the position of the continuum polarisation on the Stokes q-u plane (see Figure 3). By 0 days, the points begin to separate into two polarised clusters, at ∼20° and ∼165° for velocities $\gtrsim -8000$ km s^{-1} and $\lesssim -8000$ km s^{-1}, respectively.

At earlier epochs, the polarisation peak occurs redward of the absorption minimum, at a velocity of -6200 km s^{-1} between -10 and +7 days. The velocity at which the polarisation maximum occurs dramatically increases at later times to $-11{,}900$ km s^{-1} and $-10{,}200$ km s^{-1} at +25 and +36 days, respectively. The significant increase in the velocity of the maximum degree of polarisation is accompanied by a rotation in the polarisation angle from $\theta_{\rm line}$=20±8° at +9 days to $\theta_{\rm line}$=128±9° at +25 days. The increase in velocity and the rotation of the polarisation angle at +25 days appears to be the result of a HV component becoming more strongly polarised than the LV component (that dominated the polarisation at earlier epochs) as can be seen on Figure 1 and Figure 3.

As was observed for Ca II, the polarisation angle for He I/Na I D blend also exhibits a discontinuity at +7 and +9 days (see Figure 5). This discontinuity occurs at -9800 km s^{-1}, which is higher than the velocity of the discontinuity observed for Ca II. For He I/Na I D, the LV component has a polarisation angle of $\theta_{\rm line}$=25° and is separated by 40° from the HV component at $\theta_{\rm line}$=165° (or -15°). At +25 days, the polarisation angle is contant at ∼ 47° for velocities less than -6500 km s^{-1}, before increasing to 141° at $-14{,}000$ km s^{-1}. A similar trend is observed at +36 days.

For He I λ6678, significant polarisation is only observed at the final epoch; with $p_{\rm line}$=1.0± 0.3% and $\theta_{\rm line}$=180±9°. Conversely, polarisation is observed for He I λ7065 at 0, +9 and +36 days. The degree of polarisation of He I λ7065 reaches a maximum at +9 days with $p_{\rm line}$=0.73±0.06% and $\theta_{\rm line}$=10±2°, before undergoing a rotation in the polarisation angle to 138 ± 14° at +36 days. The lack of significant polarisation across the He I λ7065 and He I λ6678 lines at all epochs makes it difficult to determine to what degree the Na I doublet contributes to the polarisation of the He I/Na I D blend. The shape of the He I λ5876 and He I λ7065 line profiles show good agreement at 0, +7 and +9 days, which may indicate a minimal contribution from Na at these epochs. At -10, +25 and +36 days, however, the line profiles are different, with the velocity at the He I λ5876 absorption minimum being substantially higher. The agreement between the He I/Na I D and He I λ7065 polarisation angles at low velocities ($\gtrsim -4000$ km s^{-1}) suggests He dominates the polarisation signal in that velocity range.

We conclude that the HV He I component, although weakly polarised and potentially contaminated by the polarised Na I doublet, is a real feature and represents a separate line forming region for He I at high velocities. Contamination from polarised Na I D would result in a steady rotation of the polarisation angle, rather than the discontinuity observed in Figure 5.

4.3.3 *Fe* II

Peaks in the polarisation are also observed around 4700-4800 Å, coincident with an Fe II absorption trough. As such, we associate it with the nearest redward strong emission of Fe II λ4924. The strength of the polarisation grows from p=0.54±0.26% at -10 days to p=1.4±1.0% at +36 days. The uncertainty on the last measurement is large and the feature appears to be due to one elevated bin at -5000 km s^{-1}(which may indicate that the feature at +36 days is an artefact from the reduction). The Fe II λ4924 feature is polarised to the ∼0.6% level for the majority of the observations. The velocity of the maximum polarisation initially increases from -9800

km s^{-1} to $-$13,800 km s^{-1} between -10 and 0 days, before decreasing back to -9800 km s^{-1} at $+9$ days and then increasing again to $-11{,}800$ km s^{-1} at $+25$ days. The polarisation angle rotates from $\theta_{\rm line}$=83$\pm$14° in the first epoch to $\sim$135° at 0 days; it then remains approximately constant throughout the remainder of the observations.

4.3.4 *The* 6200Å *Feature*

Significant polarisation is associated with the absorption at $\sim$ 6200Å in the first two epochs, with a maximum polarisation of p=0.59$\pm$0.06% at -10 days. If this feature is due to Si II, the velocity of the polarised feature decreases from -6400 km s^{-1} to -3500 km s^{-1} between -10 and 0 days. Alternatively, if the feature is Hα then the velocities at the two epochs are, instead, $-16,400$ km s^{-1} to $-13,400$ km s^{-1}. Between -10 and 0 days, there is also a small rotation in the polarisation angle from $\theta_{\rm line}$=76$\pm$3° to $\theta_{\rm line}$=63$\pm$7°. Significant polarisation is not observed after 0 days, when the strength of the absorption feature decreases until it disappears by $+25$ days.

4.3.5 *O* I

O I λ7774 appears in the spectrum as a weak P Cygni profile from $+25$ days onwards. Upon removal of the continuum polarisation O I remains significantly polarised at $+36$ days. We estimate a polarisation associated with O I of 0.66$\pm$0.13% at -3800 km s^{-1}at $+36$ days, with $\theta_{\rm line}$=154$\pm$6°; however, this measurement is complicated by the proximity of the line to a telluric feature.

4.4 The Polarimetric Evolution in the Plane of the Sky

The measured polarisation angles provide an indication of the locations of the line forming regions for different species in the plane of the sky. Maund et al. (2009) suggested a new type of polar plot for spectropolarimetric data, that may be used to illustrate the relative positions of the different line-forming regions in radial velocity space and in the plane of the sky. These polar plots, or Maund diagrams, provide a projection of the approximate 3D structure of the SN ejecta independently of models. The spectropolarimetric observations of iPTF 13bvn are presented in this form on Figure 6.

The continuum polarisation angle is seen to rotate from $\sim$20°, before maximum light, by $\sim 90^\circ$ after maximum (i.e. moving from the top half to the lower half of the polar plot). This is indicative of a substantial change in the orientation of the asymmetry of the photosphere and hence in the underlying excitation structure powering the continuum before and after the light curve maximum.

At -10 days, the most significantly polarised features belong to Ca II, Fe II and the 6200Å. The separate species share a polarisation angle on the sky of $\theta_{\rm line}$ $\sim$70° which is misaligned with the continuum polarisation angle by $\sim$50 degrees.

At 0 days a continuous anti-clockwise rotation in the polarisation angle with increasing velocity is observed across the Ca II IR3 line profile, creating a spiral-like structure in the polar plot. Conversely, for the He I/ Na I D blend, the polarisation angle rotates clockwise across the line profile. It wraps around zero degrees (equal to a complete 180° rotation of the Stokes parameters) at approximately -8000 km s^{-1} and settles at 140-150° for velocities between $-10{,}000$ and $-15{,}000$ km s^{-1}. At low velocities ($\gtrsim -5000$ km s^{-1}) the polarisation angles for Ca II and the He I/Na I D blend, as well as that of the Si II λ6355/Hα, are similar at $\theta_{\rm line}$ $\sim$60°. At higher velocities, the polarisation angles for the two lines diverge and between $-10{,}000$ and $-15{,}000$ km s^{-1} they are offset by $\sim$70 degrees. This suggests that at low velocities the He and Ca line-forming regions occupy a similar location in the ejecta, but not at high velocities.

At $+7$ and $+9$ days, the two He I/Na I D components are still visible in the polar plot. The weighted average of the polarisation across the HV component is shaded in blue on the polar plot, where the width of the shaded region represents the standard deviation. The continuum polarisation angle at $+7$ days is aligned with Fe II and the HV ($v \lesssim -9{,}800$ km s^{-1}) portion of the He I/Na I D blend. At the same velocities, however, Ca II does not share the same orientation, being offset by $\sim$40°. At $+7$ days there is also some evidence for a further $\sim$30° rotation between Ca II at $\sim -8000 - 15,000$km s^{-1} and the V-HV Ca II component at velocities $\lesssim -15{,}000$ km s^{-1} (which tends towards the continuum polarisation angle). At $+9$ days, the Ca II line profile is now also clearly composed of two (possibly three) separate components on the polar plot. The LV components of the He I λ7065 and the He I λ5876/Na I D blend and Ca II are all aligned at $\sim 25^\circ$. At this epoch the polarisation angle of Fe II has rotated to $\sim$140°, positioned in between Ca II and He I/Na I D on the polar plot. The intrinsic continuum polarisation angle at this epoch also appears to approximately align with that of the HV Ca II and Fe II components.

Following the decline in the signal-to-noise at later epochs, the data appear more dispersed on the polar plots in the final two epochs of polarimetry ($+25$ and $+36$ days). At $+25$ days, the LV Ca II component appears to undergo an anti-clockwise rotation from $\sim$20° at $+9$ days to $\sim$70° at $+25$ days, while the HV component appears to be unchanged. At $+25$ days, the most strongly polarised features in the Fe II, Ca II and He I/ Na I D line profiles all share the same polarisation angle of $\theta_{\rm line}$ $\sim$120° and have similar velocities of $\sim -10{,}000$ km s^{-1}. These features are offset from the continuum orientation by $\sim$40°.

At $+36$ days, the polarisation angles of Fe II, Ca II, He I and O I λ7774 are approximately aligned with that of the continuum at $\sim$160°. The alignment of most of the separate species in these later epochs implies that, to some degree, the line-forming regions are shared between the different species in the plane of the sky.

4.5 Monte Carlo Simulation of the Geometry

In an effort to constrain the geometry we constructed a toy model following the procedure of Maund et al. (2010). This model was designed to compare the observed polarisation of the blue-shifted absorption components of P Cygni profiles with the polarisation induced by blocking of the continuum light by simple obscuring line-forming regions. The Monte Carlo simulation used 1×10^7 photons, distributed across a 2D elliptical photosphere with axis ratio E_P. The simulation included a spherical limb darkening model, mapped to the ellipse. Each photon was polarised according to a probability function that assigned a polarisation angle based on the position of the photon's origin from the centre of the photosphere. The photon was either assigned a random polarisation angle or a polarisation angle tangential to the ellipse at the position of the photon. Those photons closer to the limb of the photosphere were less likely to be randomly polarised. This configuration replicated the effect that photons arising from the limbs are more likely to have been scattered by 90 degrees into the line-of-sight and, hence, are more polarised. The polarisation probability function was scaled to reproduce the degree continuum polarisations predicted for pure electron scattering, oblate ellipsoids by Höflich (1991). We deter-

Figure 6. Polar plots for iPTF 13bvn from −10 to +36 days relative to the *r*-band light curve maximum. The diagrams show $\theta_{\rm line}$ as a function of the velocity (km s^{-1}; increasing radially). The polarisation angle across the line profiles for Ca II, He I/Na I D and Fe II is plotted, with the data at maximum polarisation marked with the heavy line. For other lines, just the polarisation angle and velocity at the maximum polarisation is plotted. We only show those line features that are significantly detected above the continuum level ($p > p_{cont} + 3\sigma$). The length of each arc represents the $\pm 1\sigma$ uncertainties on the polarisation angle. The photospheric velocity as measured by the velocity at the absorption minimum of Fe II λ5169 is indicated by the black dashed semi-circle, while the continuum polarisation angle is shaded in grey.

(a) The line polarisation at this epoch is characterised by a shared polarisation angle for Ca II, Fe II and Si II/Hα across a large velocity range. Indicative of a shared axis of symmetry for the line forming regions in the outer ejecta that is slightly rotated from that of the photosphere, as marked by the grey shaded region.

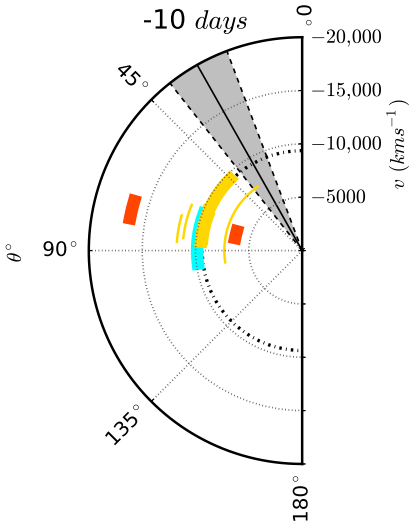

(b) The light curve maximum appears to be a transitional phase where the LV and HV components observed later begin to emerge. A rotation in the polarisation angle with velocity is observed for both Ca II (counter-clockwise) and He I/Na I D (clockwise), appearing as spirals on this plot.

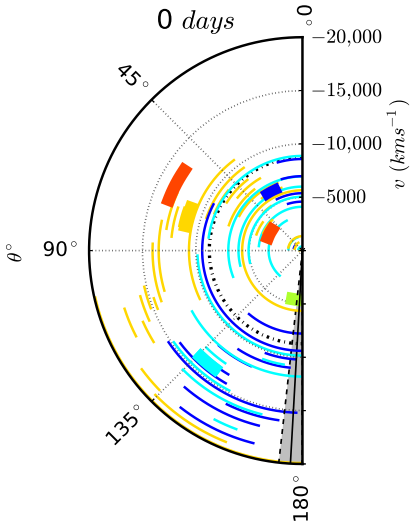

(c) The LV and HV components of He I/Na I D become more apparently distinct at +7 days. The polarisation angle of the HV He I/Na I D component is marked by the shaded blue region at this epoch and at +9 days. From +7 days onwards the continuum polarisation angle approximately aligns with the HV components.

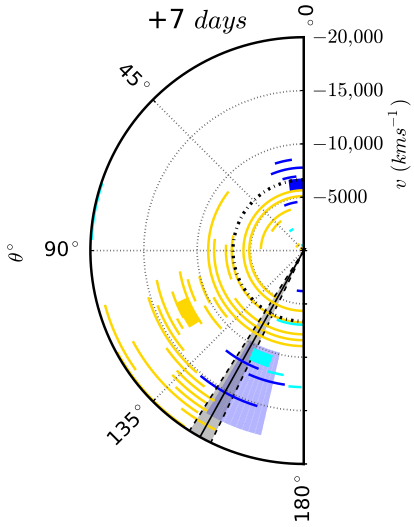

(d) The separation of the LV and HV components is most clearly seen at this epoch. LV Ca II and He I/Na I D components, moving at velocities $\gtrsim -8000$ km s^{-1}, share a polarisation angle of ∼25°. The higher velocity material show a greater dispersion among the separate ions from ∼120° to ∼170°.

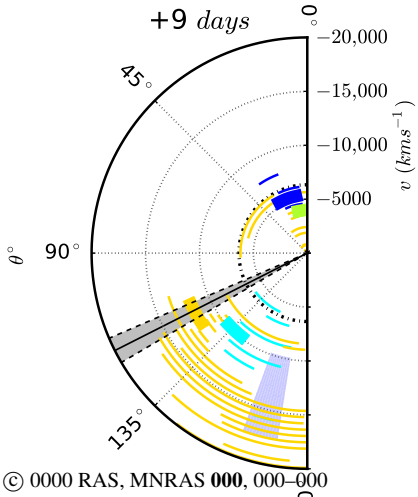

(e) Similarly to −10 days, the polarisation angles of all species approximately agree indicating an axis of symmetry for the inner ejecta in alignment with the earlier HV Ca II component.

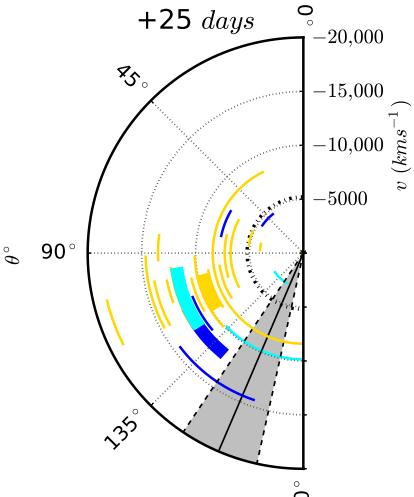

(f) A slight rotation in the line polarisation angles towards that of the continuum is observed in this final epoch of polarimetry, indicative of a shared axisymmetric geometry for the photosphere and line forming regions. Both Ca II and He I/Na I D display some scatter in the polarisation angle with velocity, suggesting that departures from this axisymmetry are also present in the ejecta at late times.

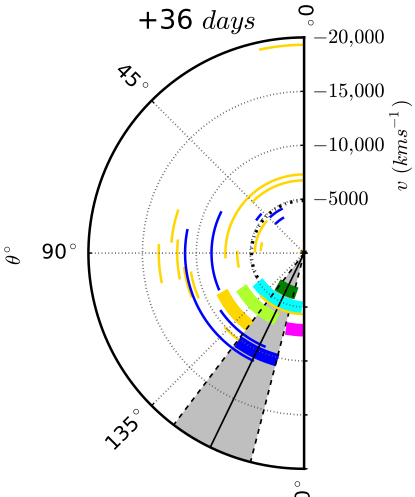

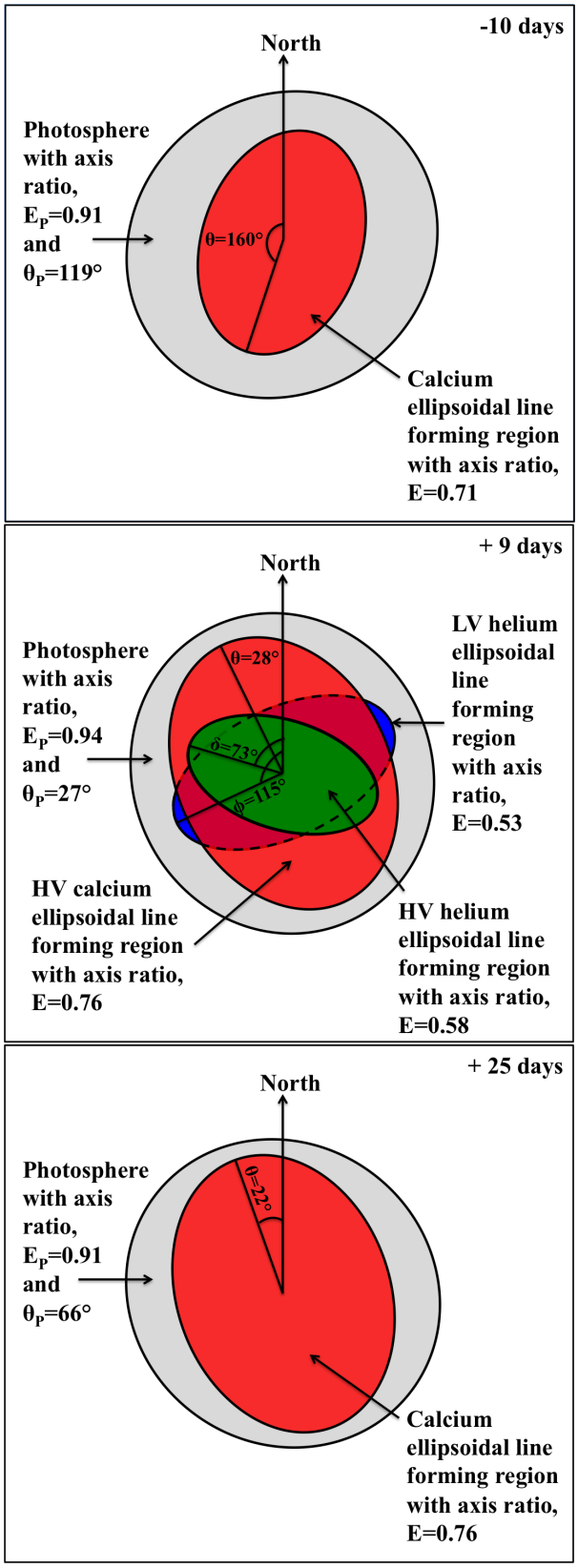
-10 days
North
Photosphere with axis ratio, E_P=0.91 and θ_P=119°
θ=160°
Calcium ellipsoidal line forming region with axis ratio, E=0.71
+ 9 days
North
Photosphere with axis ratio, E_P=0.94 and θ_P=27°
θ=28°
δ=73°
ϕ=115°
LV helium ellipsoidal line forming region with axis ratio, E=0.53
HV calcium ellipsoidal line forming region with axis ratio, E=0.76
HV helium ellipsoidal line forming region with axis ratio, E=0.58
+ 25 days
North
Photosphere with axis ratio, E_P=0.91 and θ_P=66°
θ=22°
Calcium ellipsoidal line forming region with axis ratio, E=0.76

Figure 7. A schematic of the simulated line forming regions at −10 (top), +9 (middle) and +25 days (bottom) for Ca II (red) and LV He I (blue) and HV He I (green) covering an ellipsoidal photosphere with an axis ratio, E_P and aligned with the long axis at θ_P from North (grey). The polarisation simulation was able to successfully reproduce the observed continuum and line Stokes vectors.

mined that 16.5% of limb photons were required to be polarised parallel to the photosphere edge to reproduce the expected levels of polarisation.

Simple line-forming regions were then placed over the photosphere and assumed to have large optical depth, so as to completely absorb all photons originating from the area of the photosphere covered by the line forming region. The shapes of the blocking regions used include a circle, an ellipse with varying axis ratio, rectangular boxes (such as an edge-on disk-like CSM would appear) and triangular lobes (such as bipolar outflows might appear, as viewed from the equator). The blocking regions were rotated and/or moved across the photosphere to model the degree of polarisation, the polarisation angle and the depth of the absorption component in the flux spectrum. Combinations of shapes were also modelled simultaneously to recreate more complex line forming regions. The final total Stokes parameters for each model were calculated following the same procedures used to determine the Stokes parameters from observational data. The fraction of photons absorbed by the line forming region was calculated and compared to that absorbed in one 15 Å bin in the observed flux spectrum.

This procedure was used to constrain the shape of the photosphere and principal line forming regions at 3 characteristic epochs: −10, +9 and +25 days. These epochs were chosen as they probe the outer and inner most ejecta, and the transition between the two regimes. At −10 and +25 days, we only modelled the polarisation of Ca II IR3 . At +9 days, the data show the clearest signals of separate HV and LV components of Ca II IR3 and He I, implying that any blending between the two components in the line is minimal and so the observed polarisation properties and line depth at a given velocity is solely due to one of the two components. The model was used to reproduce the observed line depth and polarisation properties at the single wavelength at which the maximum degree of polarisation for a given line of interest was observed in our data. Possible line forming region configurations that could reproduce the observed Stokes parameters were found by trial and error (see Figure 7). For all lines being considered at each of the three epochs, we found that the line polarisations could be replicated by assuming a simple ellipse for each region centred on the centre of the photosphere. These ellipses were characterised by the size of the major axis of the ellipse (relative to the major axis of the photosphere), the major to minor axis ratio and the orientation angle of the major axis of the ellipse, measured East of North.

For the data at −10 days, we found that a configuration of an ellipsoidal photosphere with E_P=0.91, with the major axis oriented at θ_P =119° reproduced the degree and angle of the continuum polarisation. Simulations of the data at +9 and +25 days required the photosphere to be rotated to θ_P =27°, but with a similar axial ratio as used for the earlier epoch.

At −10 days, the polarisation of Ca II IR3 was best reproduced with an ellipse with an axis ratio of 0.71 and major axis oriented at θ ∼160°, offset by 41° from that of the photosphere. In terms of axis ratio, the simulated HV Ca II did not undergo a significant change between −10 and +9 days, however the orientation of the region rotated by ∼130° (or −50°) to θ ∼30°. In order to recreate the larger fraction of photons absorbed by this line at +9 days, the size of the obscuring region was increased from 70% to 88% of the major axis of the photosphere.

An ellipse with a more extreme axis ratio of 0.53 was required to reproduce the observed LV component of He I/Na I D, oriented at 115° and with size 75% of the photosphere. This would imply that the LV He I component covers a substantially smaller portion of the photosphere than HV Ca II and that the degree of asymmetry is

more extreme. The polarisation properties of the HV component of He I/Na I D could also be reproduced with an elliptical line forming region with an axis ratio of 0.58. The lower absorption depth of the HV component implies that it covered less of the photosphere than the LV component, with a major axis 60% of the size of the photosphere. The principal axis of the HV component line forming region is also significantly rotated from that of the HV Ca II line forming region and the photosphere by 73° (or 42° from the LV He I/Na I D component).

The simulation indicates that neither the photosphere nor the Ca II line forming regions are subject to a dramatic change in geometry between $+9$ and $+25$ days. As there is a small scatter in the polarisation angle between all species at these epochs, it is reasonable to expect that they may all have a geometry similar to that shown in Figure 7.

We caution that while our assumption of line forming regions composed of simple shapes can reproduce the observed levels of polarisation, it does not imply that these are unique solutions nor that they are necessarily correct. In addition, the geometries for the line forming regions we have identified using our toy model are also dependent on the choice of the ISP.

5 Discussion

5.1 iPTF 13bvn in the Context of Other Stripped CCSNe

iPTF 13bvn stands out amongst the limited sample of stripped-envelope CCSNe for which there are polarimetric observations, by having such a dense time series of spectropolarimetric observations (6 epochs). The observed polarisation properties of this class of SNe are very diverse, particularly regarding the line polarisation. iPTF 13bvn shows similarities to the other stripped-core SNe, however there are also some aspects in which it exhibits significantly different behaviour.

The low levels of continuum polarisation observed here are consistent with those found in other stripped CCSNe, such as SNe 2008D, 2007gr, 2005bf, and 2002ap (Maund et al. 2009; Tanaka et al. 2008; Maund et al. 2007b; Kawabata et al. 2002). These levels of polarisation limit the degree of global asymmetries to $\lesssim$10% (Höflich 1991). A feature consistently observed in all stripped CCSNe (Maund et al. 2009), and some thermonuclear Type Ia supernovae (Mazzali et al. 2005), is the absorption trough of Ca II IR3 , which is commonly associated with high velocities ($\sim$10-20,000 $\mathrm{km\ s^{-1}}$) and large degrees of polarisation ($\sim$2-4%). This feature tends to form at higher velocities in the ejecta and with a polarisation angle that is markedly different to those of other species (Tanaka et al. 2012; Maund et al. 2009; Tanaka et al. 2008; Maund et al. 2007a,b). In addition, occasionally separate LV and HV components can be resolved in the Ca II line profile in the flux spectrum (e.g. Maund et al. 2009). Species such as He I, Fe II, O I, Si II and Na I D are frequently observed to form closer to the photosphere and with similar polarisation angles that are distinct from that of Ca II (e.g. SN 2008D Maund et al. 2009, and their Figure 11). For iPTF 13bvn, the velocity at the Ca II IR3 absorption minimum is substantially higher than that of the other species. At maximum light and a week later, the polarisation angle at maximum polarisation for Ca II IR3 is different from He I and Fe II. The multi-epoch observations here allow us to follow the temporal evolution of the polarisation associated with spectral lines. In iPTF 13bvn both Ca II and He I are observed to have photospheric and HV components that are geometrically distinct. Fe II $\lambda4924$ is also polarised at similar velocities and has a similar orientation the HV He I and Ca II line forming regions, which is unique to iPTF 13bvn.

The only Type Ib SNe with spectropolarimetric observations, other than iPTF 13bvn, are SNe 2005bf, 2008D and SN 2009jf (Maund et al. 2007b, 2009; Tanaka et al. 2012). Maund et al. (2007b) presented polarimetric observations of the unusual SN 2005bf that was originally classified as a Type Ic SN (Morrell et al. 2005), before the later appearance of He lines (Folatelli et al. 2006). For SN 2008D Maund et al. (2009) presented two epochs of spectropolarimetry at $\sim$*V*-band maximum and 15 days later. At the closest comparable epochs of 0 and $+25$ days, SN 2008D shows similarities to iPTF 13bvn in the polarisation associated with certain spectral lines. For SN 2008D, the velocities and polarisation angles at the absorption minimum of He I and Fe II lines indicates that the two species are found in similar parts of the ejecta, while Ca II is found at higher velocities and separated in polarisation angle by $\sim100^\circ$. iPTF 13bvn shows similar behaviour to SN 2008D at 0 days, where He I and Fe II are observed to have similar polarisation angles at similar velocities, while Ca II IR3 is observed at a higher velocity with a polarisation angle offset from the other species by $\sim70^\circ$. Maund et al. (2009) also observe significant polarisation associated with the O I $\lambda7774$ line, the polarisation angle of which aligns with that of high velocity Ca II at *V*-band maximum. For iPTF 13bvn, however, O I $\lambda7774$ appears much later and there is no significant polarisation associated with it until $+36$ days, at which stage the polarisation angle is aligned with the continuum and all other polarised species.

5.2 Complex Multi-axis Symmetry

The spectropolarimetric data of iPTF 13bvn have revealed the presence of multiple separately polarised components to the ejecta. The observations of loops on the q-u plane indicate that the orientation of the line forming regions for Ca II IR3and He I/Na I D change with velocity (radius). The loops observed at $+9$ days and the step-like discontinuities in the polarisation angle across the Ca II IR3 and He I/Na I D profiles at $+7$ and $+9$ days imply that there are two geometrically distinct line forming regions for the LV and the HV components.

The LV components of He I and Ca II IR3 have the same polarisation angle, implying that they form in the same location in the ejecta. These separately polarised components may suggest either two physically distinct line forming regions for both calcium and helium or a change in the underlying ionisation structure (Chugai 1992). The possible geometry of LV He I, from the Monte Carlo simulations, may then also be applicable to LV Ca II. Although we have assumed simple ellipsoidal configurations for the line forming region, and have not explored more complex geometries, we can rule out some geometric configurations. The rotation of the polarisation angle across these lines, compared to the continuum polarisation angle, shows that a shell with a similar shape to the photosphere that selectively blocks only part of the unpolarised light cannot be responsible for the observed degree of polarisation (Kasen et al. 2003). The small scatter in the polarisation angle across the LV components also suggests that this shared line forming region is a single continuous structure in the ejecta, rather than arising in clumps (Maund et al. 2010; Hole et al. 2010). In terms of the simple geometries explored in the simulation here and those presented by Kasen et al. (2003) and Hole et al. (2010), a non-clumpy elliptical line-forming region or shell, with different orientations to the asymmetry of the photosphere, can provide a reasonable explanation for the observed polarisation properties of iPTF 13bvn. Pre-

viously, Maund et al. (2007b) inferred spherical configurations for the LV line-forming regions for SN 2005bf. In addition, although the jet-torus paradigm (Khokhlov et al. 1999) has been invoked to explain spectropolarimetric observations of some stripped CCSNe (Tanaka et al. 2008), we can exclude a torus-like line-forming region for the LV components as we do not observe the high levels of polarisation predicted for such a geometry (Kasen et al. 2003).

The HV component of Ca II IR3 in iPTF 13bvn is observed to be highly polarised, with a velocity much greater than the bulk of the ejecta. For iPTF 13bvn, we observe the same polarisation angle in HV Ca II, HV He I and Fe II, which is in stark contrast to the distinctly different polarisation angle for Ca II IR3 , compared to other species, observed for SNe 2005bf, 2007gr and 2008D (Maund et al. 2007b; Tanaka et al. 2008; Maund et al. 2009). Similarly to the LV component, the polarisation properties of HV Ca II were best replicated in the polarisation simulation with an elliptical line-forming region. It is interesting to note that the presence of two velocity components for Ca II IR3 is only discernible in the spectropolarimetric data, and that these two components are not resolved in the line profile of the flux spectrum. This undermines the accuracy of our simulation, which assumes that the line depth and polarisation were due to the same line forming region. The 2D bipolar model of Tanaka et al. (2012) produces a straight line on the q-u plane which also provides a match to the observed polarisation characteristics of HV Ca. It is unclear to what degree Na I D plays a role in the He I/Na I D blend, and therefore whether He I and Ca II share the same line-forming region. The results of the polarisation simulation suggest that, likewise, an elliptical line forming region can also reproduce HV He I but that is rotated compared to HV Ca II.

In the later epochs, ($+25$ and $+36$ days) the loops on the q-u plane across the He I/Na I D blend and Ca II IR3 profile (Figure 3) appear more variable with several peaks in the degree of polarisation apparent in Figure 1. The evolution across the line is reminiscent of those generated in the simulations by Hole et al. (2010), where the ejecta are composed of clumps separated in velocity space. This suggests that the ejecta, while apparently still following a principal axis of symmetry, develop a degree clumpiness at later times. At -10 days, the line polarisation of the LV and HV component share similar polarisation angles consistent with a single axial symmetry, with no evidence of clumpiness within the ejecta. The implication is that between $+9$ and $+25$ days the ejecta became clumpy, most likely due to hydrodynamic instabilities. Such instabilities could propagate through the ejecta (Blondin & Ellison 2001) or may develop from remnant asphericities in the explosion mechanism itself, such as the standing accretion shock instability (Janka et al. 2007) or through the propagation of a jet-like flow through the progenitor star (Couch et al. 2009, see also Wheeler et al. 2008 for discussion of jet-induced hydrodynamical instabilities in SNR Cas A and Hammer et al. 2010 for simulations of instabilities in supernova explosions).

There are no previous observations of two geometrically and physically distinct He I line forming regions in the ejecta of Type Ib SNe. The properties of both the HV and LV components for iPTF 13bvn are different from those observed for other stripped CCSNe. It is possible that the scarcity of previous polarimetric observations or viewing angle effects may have meant that this feature has been missed in the other SNe. If these features are truly unique to iPTF 13bvn, signs of the SN's peculiarity may be expected in the light curve or spectra. iPTF 13bvn was classified as a Type Ib SNe, with similarities to SN2009jf, while the light curve was observed to be fast declining and of low luminosity (Srivastav et al. 2014). It is possible that the observations of the two He I components are related to the plateau in the evolution of the He I velocity (see Fig. 2). A similar plateau is also observed in SN 2008D (see Modjaz et al. 2009, and their Figure 13), however the polarised HV and LV components in Ca II and He I observed in iPTF 13bvn are not seen in SN 2008D (Maund et al. 2009). Only increasing the sample of Type Ib SNe with high polarimetric coverage can resolve the question of whether this complex ejecta morphology is common to all Type Ib SNe or only a subset, and what role the explosion mechanism plays in the formation of these multiple components.

5.3 Non-thermal excitation

The velocity at the absorption minimum of the He I/Na I D blend is observed to decay steeply before plateauing at around maximum light (see Figure 2). The velocities measured for the He I $\lambda 6678, 7065$ lines also appear to plateau at the same time (see Fremling et al. 2014, and their Figure 6). The plateau in the He I velocity may arise from non-thermal excitation, from the direct deposition of gamma rays from the radioactive decay of ^{56}Ni and ^{56}Co, at velocities higher than the photospheric velocity (Lucy 1991). The geometry of He I may, therefore, serve to trace the geometry of the radioactive nickel. The coincident emergence of the HV and LV components in the polarimetry with the beginning of the He velocity plateau at $\sim$ maximum light suggests that the non-thermal excitation of the He I lines also powers those components.

In principle, the collision of an approximately spherical ejecta with an aspherical circumstellar medium (CSM) could also produce the observed early evolution in the polarimetry. If interaction were the dominant source of non-thermal excitation, we might expect to also see narrow emission lines in the spectrum, which are not seen in our observations of iPTF 13bvn. Furthermore, the collision of ejecta and a CSM would result in an injection of energy, identifiable in the light curve as a decline that is slower than expected from radioactive decay. Srivastav et al. (2014) note, however, that iPTF 13bvn has a faster decline than most Type Ib/c SNe and faster than expected for the decay of ^{56}Co. This suggests a deficiency of energy in the ejecta due to incomplete trapping of gamma rays as opposed to energy from interaction with the CSM. The observations, therefore, disfavour interaction as the source of the separate components and the He I velocity plateau and are, instead, consistent with ^{56}Ni located above the photosphere at and after the light curve maximum. The photospheric velocity measured at 18 days post-explosion reveals that nickel must be mixed out to $\sim$50-65% of the ejecta, by radius, at $\sim$8700 $\mathrm{km\ s^{-1}}$. Bersten et al. (2014) performed one dimensional hydrodynamical explosion models of iPTF 13bvn which required ^{56}Ni to be mixed out to $\sim$96% of the initial mass of the progenitor to reproduce the observed rise time of the light curve. The discrepancy between these two estimates for the degree of Ni mixing most likely arise in the application of a 1D model assuming spherical symmetry to, as we have observed, an asymmetrical situation. If the polarisation of the HV and LV He I components at $+7$ and $+9$ days trace the 2D projected distribution of nickel, this implies that not only is it not spherically distributed, covering only a portion of the photosphere, but also that it is distributed in at least two (if not more) outflows originating from the core. Our observations have demonstrated the importance of spectropolarimetry for measuring how Ni is mixed into the outer layers of the SN ejecta and the degree of this mixing. This has important implications for how photometric and spectroscopic observations are interpreted, especially in the context of 1D models.

5.4 Implications for the Explosion Geometry

The absence of any strong O I lines in the spectrum until $+25$ days indicates that the core is still shielded by the photosphere until that epoch. The presence and polarisation of He I, at $\sim$ maximum light, indicates the role of non-thermal excitation from Ni deposited above the core by an axisymmetric outflow that stalled in the helium mantle.

The approximate alignment of the continuum polarisation angle in the later epochs ($+25$ and $+36$ days) with that of the HV component suggests that there is a principal axis of symmetry for the explosion which may lend itself to the interpretation of a bipolar or jet driven explosion. In this model a jet, originating either from asymmetric neutrino emission (Blondin & Mezzacappa 2007) or the magneto-rotational mechanism (LeBlanc & Wilson 1970; Mikami et al. 2008), would carry heavy elements in bipolar flows, while low and intermediate mass elements (e.g. helium and oxygen) would form a torus in the equatorial plane (Khokhlov et al. 1999; Khokhlov & Höflich 2001; Maeda et al. 2002). We observed no such segregation between the locations of heavier mass (iron and calcium) and lower mass (helium and oxygen) elements in the ejecta, that would suggest such a geometric configuration for iPTF 13bvn. The presence of a separate LV component of He I, which must also arise from non-thermal excitation, also implies that the distribution of nickel cannot be described by just a simple bipolar geometry.

In comparison with the velocity of the HV He component (~ -8700 km s^{-1}) which we use as a tracer for the Ni distribution, the high velocities ($\sim -13{,}000$ km s^{-1}) measured for Fe II lines at early times implies these features arise from primordial iron already present in the envelope of the progenitor. Likewise, the low velocity inferred for the Ni makes it improbable that the Ca II IR3 HV component traces a fast moving jet. The deposition of nickel outside of the photosphere, at $\sim$ maximum light, would lead to significant losses of gamma ray photons, which would otherwise be trapped in the ejecta under the photosphere. This could explain the low luminosity and fast light curve decline of iPTF 13bvn (Srivastav et al. 2014), and may also imply that the nickel mass derived from the bolometric light curve (0.05-0.1M$_\odot$ Srivastav et al. 2014; Bersten et al. 2014) may underestimate the true value.

Previously, the action of bipolar flows has been inferred from spectropolarimetry of other CCSNe. Tanaka et al. (2008) observed HV Ca in the Type Ic SN 2007gr, which they proposed was formed in a bipolar outflow, with oxygen distributed in a torus in the equatorial plane. Polarisation in the wavelength region around the Ca II IR3 in the Type Ic SN 2002ap was interpreted by Kawabata et al. (2002) as indicating the presence of a relativistic jet ($0.115c$) that had punched through the ejecta. Later Wang et al. (2003) presented 3 epochs of spectropolarimetry of SN 2002ap and challenged this interpretation, suggesting the polarisation was associated with oxygen at much lower velocities and suggested the data were consistent with a bipolar jet-like flow that had stalled in the core. Similarly, Maund et al. (2009) invoked a thermal energy dominated jet-like flow, that had stopped within the core, to explain the orthogonality between the polarisation angle of HV Ca II with the angles of helium and iron at lower velocities in the Type Ib SN 2008D. Maund et al. (2007b) also favoured a jet, that stopped above the core in the helium mantle, for the Type Ib/c SN 2005bf. Mauerhan et al. (2015) also favour plumes of radioactive nickel to explain the polarisation of the Type IIb SN 2011dh. Maund et al. (2009) and Wang et al. (2003) predicted that, as the photosphere recedes through the deeper layers, later observations of Type Ibc SNe would reveal evidence of an asymmetric flow originating from the explosion. Our multi-epoch spectropolarimetry of iPTF 13bvn has confirmed these predictions. Although there are differences between iPTF 13bvn and these other Type Ibc SNe, overall a consistent picture of the geometry of these events is emerging.

The geometrical properties inferred here are reminiscent of the complex morphology of the Galactic Type IIb SN remnant Cas A. The presence of the opposing North East "jet" and South West "counter-jet" are indicative of axisymmetric bipolar flows associated with the explosion, similar to that inferred here for the observations at later epochs. Several authors agree, however, that these so-called "jets" are secondary features, perhaps arising due to instabilities (Wheeler et al. 2008), accretion onto a neutron star (Janka et al. 2005) or due to precession of the axis of rotation when the bipolar flows were launched (Burrows et al. 2005). Similarly, Milisavljevic & Fesen (2013) conclude that while the observed jets are unlikely to be the result of a jet-induced explosion they are intrinsic to the explosion. Wheeler et al. (2008) proposed a model in which the jet-induced explosion launched products from explosive nucleosynthesis in a jet in the South East direction, not along the NE/SW axis. Blondin et al. (2001) and Milisavljevic & Fesen (2013) interpreted the presence of several large ejecta rings surrounding iron rich ejecta to be due to the non-axisymmetric deposition of nickel in clumps in the explosion and such a scenario has also been proposed for SN 1987A (Li et al. 1993). The inference of two outflows of nickel and additional "clumps" or "bubbles" of nickel in iPTF 13bvn may therefore have very real analogues in resolved SN remnants like Cas A (Milisavljevic & Fesen 2015).

5.5 Polarimetric Evolution and the Implications for the Progenitor System

The possible identification of a progenitor candidate for iPTF 13bvn, as reviewed in Section 1, has generated debate over the progenitor system that gave rise to this SN. For iPTF 13bvn, we have identified 3 main axes of symmetry over the period covered by our spectropolarimetric observations corresponding to: the HV component at $+9$ days and the line and continuum polarisation in the later epochs at $\sim$135°; the LV component at +9 days at $\sim$25° degrees; and the alignment of the line polarisation angles of multiple species at the earliest epoch of -10 days at $\sim$75°. The asymmetries in the earlier epochs reflect the shape of the the outer most layers of the ejecta. The difference in the polarisation angles observed at -10 days and those at later epochs ($+25$ and $+36$ days) suggests that the outer layers of the ejecta did not share the same geometry as the explosion. This suggests, similarly to what has been observed for Type IIP SNe arising red supergiant progenitors (Leonard et al. 2006; Chornock et al. 2010), that the envelope of the pre-supernova star must have been sufficiently large in order to conceal the inner explosion asymmetries for 18 days (until 0 days when evidence of the inner explosion geometry began to emerge).

In the context of understanding the origin of the geometry of the outermost ejecta, the identification of the polarised absorption feature at $\sim$6200 Å becomes especially interesting. The feature is significantly polarised in the first two epochs only (-10 and 0 days) before both the degree of polarisation and absorption depth decrease. As has been suggested for other Type Ib SNe (Wheeler et al. 1994; Deng et al. 2000; Branch et al. 2002; Parrent et al. 2015), if this features is Hα at $-16{,}400$ km s^{-1}, this would imply that the H line-forming region lies in the outermost layers of the ejecta. The polarisation of this feature may then reflect asymmetries in the out-

ermost layers of the progenitor or the progenitor's wind swept up by the ejecta.

The shape of the outer layers of the SN ejecta is also subject to the geometry of the shock break out, which is dependent upon the geometry of the explosion and dynamics of the interaction of the shock front as it propagates through the progenitor star. The post-maximum polarisation properties indicate that the explosion of iPTF 13bvn was highly asymmetric. Matzner et al. (2013) performed calculations which showed that the resulting shock front of an aspherical explosion may emerge at an oblique angle to the stellar surface. A key prediction of these models is this would induce large asphericities in the highest velocity material and hence significant polarisation. At later times the polarisations angles are then predicted to rotate, as the geometry becomes progressively dominated by the shape of the explosion mechanism, as we have observed for iPTF 13bvn. The emergence of the explosion geometry at 0 days (18 days post-explosion) implies the progenitor of iPTF 13bvn must have had a relatively extended envelope, which argues against oblique shock break out as the source of the early polarisation that Matzner et al. (2013) determined is more easily produced by compact progenitors, such as WR stars.

The early polarisation may also arise in a distorted stellar envelope. Tidal distortion of the progenitor star as a result of binary interaction has been discussed as the source of the observed polarisation in SN 1993J and recently in SN 2011dh by Mauerhan et al. (2015). Tran et al. (1997) and Trammell et al. (1993) observed high levels of continuum polarisation in SN 1993J, of $p \sim$1-2% which exhibited no strong temporal dependence. Höflich (1995) found that this could be produced by an oblate model with an axis ratio of 0.6, while Tran et al. and Trammell et al. argued that the lack of strong temporal change in the polarisation was an indication that the asymmetry was not intrinsic to the explosion but due to a distorted envelope. The strong asphericity was linked to a pre-SN common envelope phase in a close binary system (Höflich 1995). Similar polarisation properties were observed for SN 1996cb (Wang et al. 2001) and SN 2001ig (Maund et al. 2007), with Maund et al. suggesting that they were the result of a similar binary progenitor system. The alignment of the Ca II IR3, Fe II and Si II polarisation angles and the non-zero degree of continuum polarisation ($\sim$0.2-0.7% depending on the chosen ISP) suggests that the envelope was distorted in an axisymmetric manner. The effect of the tidal distortion of the progenitor on the early-time polarisation of the SN may be amplified by how the explosive shock is able to propagate through the distorted star. Fast rotation or tidal interaction with a binary companion leads to a density profile in the progenitor that is steeper along the direction of the poles. Steinmetz & Höflich (1992) showed that a spherical shock front would take on a prolate shape upon encountering the steeper density gradient along the poles. For a massive, differentially rotating star (like the progenitor of SN 1987A), Steinmetz & Höflich found that at $\sim$ 30 days post explosion the photosphere receded through the oblate ejecta to the prolate regions, producing a rotation of the polarisation angles. The observations of iPTF 13bvn are also roughly consistent with this model.

Spectropolarimetric surveys of galactic and Large Magellenic Cloud (LMC) Wolf-Rayet stars show that the majority ($\sim$80%) are slow rotating spherically symmetric stars (Harries et al. 1998; Vink 2007; St-Louis 2011). Based on geometry alone, the progenitor of iPTF 13bvn is unlikely to have been a slowly rotating WR star. Vink et al. (2011) and Gräfener et al. (2012) discovered that a subset of WR stars that were rotating sufficiently fast to result in a flattened wind were also associated with ejecta nebulae, such that they concluded that these had to be young WR stars (having recently been through a luminous blue variable or red supergiant phase). In low metallicity environments the line-driven winds of these fast rotators will be too weak to remove significant amounts of angular momentum (Yoon & Langer 2005), such that they would retain any rotational induced asymmetries up to the point of explosion. Vink (2007) proposed that this effect was at most limited to metallicities below that of the LMC. Kuncarayakti et al. (2015) measured the metallicity of the region of iPTF 13bvn as being slightly subsolar, which would suggest as WR star in this region would not be expected to explode as a distorted, fast rotator.

In summary, our polarimetric observations favour an extended, distorted progenitor (possibly with residual H in the outer layers) rather than a compact WR star.

6 Conclusions

We find iPTF 13bvn to have exhibited significant continuum and line polarisation in observations covering the period from -10 to $+36$ days, with respect to the *r*-band light curve maximum. The continuum was intrinsically polarised at the 0.2-0.4% level throughout the observations, implying asphericities of $\sim$10% in the shape of the photosphere. The degree and angle of continuum polarisation was found to be dependent on the choice of the ISP.

Significant polarisation was found to be associated with the absorption profiles of spectral lines of Ca II IR3, He I/Na I D, He I $\lambda\lambda 6678, 7065$, Fe II $\lambda 4924$, Si II $\lambda 6355$ and O I $\lambda 7774$. The Ca II IR3 absorption showed the strongest degree of polarisation of $\sim$3% at $+25$ days. The polarisations of the He I/Na I D and Fe II reached maximum levels of $\sim$1%, followed by O I and Si II at $\sim$0.6%. We propose that the observation of two loops on the q-u plane associated with the He I/Na I D profile at $+7$ and $+9$ days indicates the presence of at least two physically distinct components to the ejecta. The formation of separate loops due to the blending of Na I D with He I was considered unlikely due to the sharp discontinuity observed in the polarisation angle across the profile and the lack of evidence of a strong contribution to the blend from Na I D at $+7$ and $+9$ days. Both loops are attributed to He I. Similarly, Ca II also show a "step-function"-like trend in the evolution of the polarisation angle with velocity, supporting the interpretation of at least two distinct line forming regions for He I and Ca II in the ejecta. The LV components of Ca II and He I were found to share the same polarisation angle implying a shared line forming region for the two ions. The HV components were observed with polarisation angles separated by $\sim 40^{\circ}$.

The simultaneous emergence of the HV and LV components in the polarisation data with the onset of the He velocity plateau indicated the presence of non-thermal excitation. The polarisation of the HV and LV He I components was used to trace the 2D projected distribution of nickel in the ejecta, and suggests the presence of at least two outflows originating from the core. We are able to constrain the bulk of nickel to lie interior to $\sim$50-65% of the ejecta radius, at a velocity of $\lesssim$8700 km s^{-1}. This is in disagreement with the prediction from 1D hydrodynamical models, requiring mixing out to $\sim$96% of the initial mass of the progenitor to reproduce the observed rise time of the light curve.

The approximate alignment of the continuum polarisation angle in the later epochs with that of the HV component suggests that there was a main axis of symmetry in the explosion, which could be consistent with a bipolar or jet-driven explosion. The high quality of our data reveal, however, that the structure of the ejecta is

not just described by a simple, single axial symmetry and that the morphology of the explosion is much more complicated. Other outflows, originating from the explosion, appear to have been launched in multiple directions but, similarly to other Type Ib SNe, stalled in the He mantle of the progenitor star. The structure of the outer layers of the ejecta are consistent with a rotationally supported, non-WR star that had retained a thin shell of H at the time of explosion. Our spectropolarimetric observations of iPTF 13bvn have revealed a complex explosion geometry that is reminiscent of that observed in the Galactic SN remnant Cas A.

7 Acknowledgements

ER is supported through a PhD studentship awarded by the Department of Education and Learning of Northern Ireland. The research of JRM is supported through a Royal Society University Research Fellowship. JCW is supported by NSF Grant AST 11-09881. JMS is supported by an NSF Astronomy and Astrophysics Postdoctoral Fellowship under award AST-1302771. The authors are grateful to the ESO for the generous allocation of observing time. They especially thank the staff of the Paranal Observatory for their competent and never-tiring support of this project in service mode.

REFERENCES

Appenzeller I., Fricke K., Fürtig W., Gässler W., Häfner R., Harke R., Hess H.-J., Hummel W., Jürgens P., Kudritzki R.-P., Mantel K.-H., Meisl W., 1998, The Messenger, 94, 1

Bersten M. C., Benvenuto O. G., Folatelli G., Nomoto K., Kuncarayakti H., Srivastav S., Anupama G. C., Quimby R., Sahu D. K., 2014, AJ, 148, 68

Blondin J. M., Borkowski K. J., Reynolds S. P., 2001, ApJ, 557, 782

Blondin J. M., Ellison D. C., 2001, ApJ, 560, 244

Blondin J. M., Mezzacappa A., 2007, Nature, 445, 58

Branch D., Benetti S., Kasen D., Baron E., Jeffery D. J., Hatano K., Stathakis R. A., Filippenko A. V., Matheson T., Pastorello A., Altavilla G., Cappellaro E., Rizzi L., Turatto M., Li W., Leonard D. C., Shields J. C., 2002, ApJ, 566, 1005

Burrows A., 2013, Reviews of Modern Physics, 85, 245

Burrows A., Walder R., Ott C. D., Livne E., 2005, in Humphreys R., Stanek K., eds, The Fate of the Most Massive Stars Vol. 332 of Astronomical Society of the Pacific Conference Series, Rotating Core Collapse and Bipolar Supernova Explosions. p. 350

Cao Y., Kasliwal M. M., Arcavi I., Horesh A., Hancock P., Valenti S., Cenko S. B., Kulkarni S. R., Gal-Yam A., Gorbikov E., Ofek E. O., Sand D., Yaron O., 2013, ApJL, 775, L7

Chornock R., Filippenko A. V., Li W., Silverman J. M., 2010, ApJ, 713, 1363

Chugai N. N., 1992, Soviet Astronomy Letters, 18, 168

Couch S. M., Wheeler J. C., Milosavljević M., 2009, ApJ, 696, 953

Deng J. S., Qiu Y. L., Hu J. Y., Hatano K., Branch D., 2000, ApJ, 540, 452

Eldridge J. J., Fraser M., Maund J. R., Smartt S. J., 2015, MNRAS, 446, 2689

Folatelli G., Contreras C., Phillips M. M., Woosley S. E., Blinnikov S., Morrell N., Suntzeff N. B., Lee B. L., Hamuy M., González S., Krzeminski W., Roth M., Li W., Filippenko A. V., Foley R. J., Freedman W. L., Madore B. F., 2006, ApJ, 641, 1039

Fremling C., Sollerman J., Taddia F., Ergon M., Valenti S., Arcavi I., Ben-Ami S., Cao Y., Cenko S. B., Filippenko A. V., Gal-Yam A., Howell D. A., 2014, A&A, 565, A114

Gräfener G., Vink J. S., Harries T. J., Langer N., 2012, A&A, 547, A83

Groh J. H., Georgy C., Ekström S., 2013, A&A, 558, L1

Hammer N. J., Janka H.-T., Müller E., 2010, ApJ, 714, 1371

Harries T. J., Hillier D. J., Howarth I. D., 1998, MNRAS, 296, 1072

Höflich P., 1991, A&A, 246, 481

Höflich P., 1995, ApJ, 440, 821

Hole K. T., Kasen D., Nordsieck K. H., 2010, ApJ, 720, 1500

Janka H.-T., 2012, Annual Review of Nuclear and Particle Science, 62, 407

Janka H.-T., Langanke K., Marek A., Martínez-Pinedo G., Müller B., 2007, Phys. Rep., 442, 38

Janka H.-T., Scheck L., Kifonidis K., Müller E., Plewa T., 2005, in Humphreys R., Stanek K., eds, The Fate of the Most Massive Stars Vol. 332 of Astronomical Society of the Pacific Conference Series, Supernova Asymmetries and Pulsar Kicks — Views on Controversial Issues. p. 363

Kasen D., Nugent P., Wang L., Howell D. A., Wheeler J. C., Höflich P., Baade D., Baron E., Hauschildt P. H., 2003, ApJ, 593, 788

Kawabata K. S., Jeffery D. J., Iye M., Ohyama Y., Kosugi G., Kashikawa N., Ebizuka N., Sasaki T., Sekiguchi K., Nomoto K., Mazzali P., Deng J., Maeda K., Umeda H., Aoki K., Saito Y., Takata T., Yoshida M., Asai R., Inata M., 2002, ApJL, 580, L39

Khokhlov A., Höflich P., 2001, in Chang H.-Y., Lee C.-H., Rho M., Yi I., eds, Explosive Phenomena in Astrophysical Compact Objects Vol. 556 of American Institute of Physics Conference Series, Jet induced supernovae: Hydrodynamics and observational consequences. pp 301–312

Khokhlov A. M., Höflich P. A., Oran E. S., Wheeler J. C., Wang L., Chtchelkanova A. Y., 1999, ApJL, 524, L107

Kuncarayakti H., Maeda K., Bersten M. C., Folatelli G., Morrell N., Hsiao E. Y., González-Gaitán S., Anderson J. P., Hamuy M., de Jaeger T., Gutiérrez C. P., Kawabata K. S., 2015, ArXiv e-prints

Law N. M., Kulkarni S. R., Dekany R. G., Ofek E. O., Quimby R. M., Nugent P. E., Surace J., Grillmair C. C., Bloom J. S., Kasliwal M. M., Bildsten L., Brown T., Cenko S. B., Ciardi D., Croner E., Djorgovski S. G., van Eyken J., Filippenko A. V., Fox D. B., 2009, PASP, 121, 1395

LeBlanc J. M., Wilson J. R., 1970, ApJ, 161, 541

Leonard D. C., Filippenko A. V., Ganeshalingam M., Serduke F. J. D., Li W., Swift B. J., Gal-Yam A., Foley R. J., Fox D. B., Park S., Hoffman J. L., Wong D. S., 2006, Nature, 440, 505

Li H., McCray R., Sunyaev R. A., 1993, ApJ, 419, 824

Lucy L. B., 1991, ApJ, 383, 308

Maeda K., Nakamura T., Nomoto K., Mazzali P. A., Patat F., Hachisu I., 2002, ApJ, 565, 405

Matzner C. D., Levin Y., Ro S., 2013, ApJ, 779, 60

Mauerhan J. C., Williams G. G., Leonard D. C., Smith P. S., Filippenko A. V., Smith N., Hoffman J. L., Huk L., Clubb K. I., Silverman J. M., Cenko S. B., Milne P., Gal-Yam A., Ben-Ami S., 2015, ArXiv e-prints

Maund J. R., Wheeler J. C., Baade D., Patat F., Höflich P., Wang L., Clocchiatti A., 2009, ApJ, 705, 1139

Maund J. R., Wheeler J. C., Patat F., Baade D., Wang L., Höflich P., 2007a, A&A, 475, L1

Maund J. R., Wheeler J. C., Patat F., Baade D., Wang L., Höflich

P., 2007b, MNRAS, 381, 201
Maund J. R., Wheeler J. C., Patat F., Wang L., Baade D., Höflich P. A., 2007, ApJ, 671, 1944
Maund J. R., Wheeler J. C., Wang L., Baade D., Clocchiatti A., Patat F., Höflich P., Quinn J., Zelaya P., 2010, ApJ, 722, 1162
Mazzali P. A., Benetti S., Altavilla G., Blanc G., Cappellaro E., Elias-Rosa N., Garavini G., Goobar A., Harutyunyan A., Kotak R., Leibundgut B., Lundqvist P., Mattila S., Mendez J., Nobili S., Pain R., Pastorello A., 2005, ApJL, 623, L37
Mikami H., Sato Y., Matsumoto T., Hanawa T., 2008, ApJ, 683, 357
Milisavljevic D., Fesen R. A., 2013, ApJ, 772, 134
Milisavljevic D., Fesen R. A., 2015, Science, 347, 526
Modjaz M., Li W., Butler N., Chornock R., Perley D., Blondin S., Bloom J. S., Filippenko A. V., Kirshner R. P., Kocevski D., Poznanski D., Hicken M., Foley R. J., Stringfellow G. S., Berlind P., 2009, ApJ, 702, 226
Morrell N., Hamuy M., Folatelli G., Contreras C., (Carnegie Supernova P., 2005, IAUC, 8509, 2
Parrent J. T., Milisavljevic D., Soderberg A. M., Parthasarathy M., 2015, ArXiv e-prints
Patat F., Romaniello M., 2006, PASP, 118, 146
Quinn J. L., Baade D., Clocchiatti A., Höflich P., Maund J., Patat F., Wang L., Wheeler J. C., Zelaya P., 2012, in Hoffman J. L., Bjorkman J., Whitney B., eds, American Institute of Physics Conference Series Vol. 1429 of American Institute of Physics Conference Series, Bayesian polarization measurements. pp 274–277
Schlafly E. F., Finkbeiner D. P., 2011, ApJ, 737, 103
Silverman J. M., Vinkó J., Marion G. H., Wheeler J. C., Barna B., Szalai T., Mulligan B. W., Filippenko A. V., 2015, MNRAS, 451, 1973
Srivastav S., Anupama G. C., Sahu D. K., 2014, MNRAS, 445, 1932
St-Louis N., 2011, in Bastien P., Manset N., Clemens D. P., St-Louis N., eds, Astronomical Polarimetry 2008: Science from Small to Large Telescopes Vol. 449 of Astronomical Society of the Pacific Conference Series, Polarization of Wolf-Rayet and Other Hot, Massive Stars. p. 313
Steinmetz M., Höflich P., 1992, A&A, 257, 641
Tanaka M., Kawabata K. S., Hattori T., Mazzali P. A., Aoki K., Iye M., Maeda K., Nomoto K., Pian E., Sasaki T., Yamanaka M., 2012, ApJ, 754, 63
Tanaka M., Kawabata K. S., Maeda K., Hattori T., Nomoto K., 2008, ApJ, 689, 1191
Trammell S. R., Hines D. C., Wheeler J. C., 1993, ApJL, 414, L21
Tran H. D., Filippenko A. V., Schmidt G. D., Bjorkman K. S., Jannuzi B. T., Smith P. S., 1997, PASP, 109, 489
Vink J. S., 2007, A&A, 469, 707
Vink J. S., Gräfener G., Harries T. J., 2011, A&A, 536, L10
Wang L., Baade D., Höflich P., Wheeler J. C., 2003, ApJ, 592, 457
Wang L., Howell D. A., Höflich P., Wheeler J. C., 2001, ApJ, 550, 1030
Wang L., Wheeler J. C., 2008, ARA&A, 46, 433
Wheeler J. C., Harkness R. P., Clocchiatti A., Benetti S., Brotherton M. S., Depoy D. L., Elias J., 1994, ApJL, 436, L135
Wheeler J. C., Johnson V., Clocchiatti A., 2015, MNRAS, 450, 1295
Wheeler J. C., Maund J. R., Couch S. M., 2008, ApJ, 677, 1091
Yoon S.-C., Langer N., 2005, A&A, 443, 643